JGR Space Physics

RESEARCH ARTICLE
10.1029/2021JA030008

Special Section:
Geospace multi-point observations in Van Allen Probes and Arase era

Flux Enhancements of Field-Aligned Low-Energy O^+ Ion (FALEO) in the Inner Magnetosphere: A Possible Source of Warm Plasma Cloak and Oxygen Torus

M. Nosé[1], A. Matsuoka[2], Y. Miyoshi[1], K. Asamura[3], T. Hori[1], M. Teramoto[4], I. Shinohara[3], M. Hirahara[1], C. A. Kletzing[5], C. W. Smith[6], R. J. MacDowall[7], H. E. Spence[6], G. D. Reeves[8], and J. W. Gjerloev[9]

[1]Institute for Space-Earth Environmental Research, Nagoya University, Nagoya, Japan, [2]Graduate School of Science, Kyoto University, Kyoto, Japan, [3]Institute of Space and Astronautical Science, Japan Aerospace Exploration Agency, Sagamihara, Japan, [4]Department of Space Systems Engineering, Kyushu Institute of Technology, Kitakyusyu, Japan, [5]Department of Physics and Astronomy, University of Iowa, Iowa City, IA, USA, [6]Institute for the Study of Earth, Oceans, and Space, University of New Hampshire, Durham, NH, USA, [7]Solar System Exploration Division, Goddard Space Flight Center, Greenbelt, MD, USA, [8]Space Sciences and Applications Group, Los Alamos National Laboratory, Los Alamos, NM, USA, [9]Johns Hopkins University Applied Physics Laboratory, Laurel, MD, USA

Abstract Flux enhancements of field-aligned low-energy O^+ ion (FALEO) are simultaneously observed by Arase, Van Allen Probes A and B in the nightside inner magnetosphere during 05–07 UT on September 22, 2018. FALEOs appear after a magnetic dipolarization signature with approximately 6–20 min delay. It has the energy-dispersion signature from a few keV to ~100 eV only in the direction parallel to the magnetic field at Arase, while it decreases its energy from a few keV down to 10 eV in both the parallel and antiparallel directions at Probes A and B. We perform a numerical simulation to trace trajectories of test O^+ ions in a model magnetosphere, which are launched from above the ionosphere 3–15 min after a substorm. Flying virtual satellites that have the same orbits as the real satellites, we create virtual energy-time spectrograms of O^+ ions to compare with the observed ones. Results show a very good correspondence between them, indicating that FALEOs originate from ionospheric O^+ ions that are extracted from the upper ionosphere at substorm onset and flow along the magnetic field toward the geomagnetic equator. It is also revealed that 3–9 hr after their launch, test O^+ ions less than 400 eV have a spatial distribution in the inner magnetosphere which is similar to those of the warm plasma cloak and the oxygen torus. We therefore conclude that FALEO is a source of those cold ion populations.

Key Points:

- Flux enhancements of field-aligned low-energy O^+ ion (FALEO) are simultaneously observed by Arase, Van Allen Probes A and B
- Numerical simulation well reproduces observed energy-time spectrograms of FALEO with the energy-dispersed signature from 1 keV to 10 eV
- FALEO is a source of the warm plasma cloak and the oxygen torus that appear in the dawn to noon sectors

Supporting Information:

Supporting Information may be found in the online version of this article.

Correspondence to:

M. Nosé,
nose.masahito@isee.nagoya-u.ac.jp

Citation:

Nosé, M., Matsuoka, A., Miyoshi, Y., Asamura, K., Hori, T., Teramoto, M., et al. (2022). Flux enhancements of field-aligned low-energy O^+ ion (FALEO) in the inner magnetosphere: A possible source of warm plasma cloak and oxygen torus. *Journal of Geophysical Research: Space Physics*, *127*, e2021JA030008. https://doi.org/10.1029/2021JA030008

Received 1 OCT 2021
Accepted 1 MAR 2022

Author Contributions:

Conceptualization: M. Nosé
Data curation: A. Matsuoka, Y. Miyoshi, K. Asamura, T. Hori, M. Teramoto, I. Shinohara, C. A. Kletzing, C. W. Smith, R. J. MacDowall, H. E. Spence, G. D. Reeves, J. W. Gjerloev
Formal analysis: M. Nosé
Investigation: M. Nosé
Methodology: M. Nosé, Y. Miyoshi, T. Hori, M. Hirahara

1. Introduction

It has been reported by a number of recent studies that unidirectional/bidirectional energy-dispersed O^+ flux enhancement occurs a few minutes after substorms in the inner magnetosphere and lasts for >10 min with a decrease in its energy from ~5 keV to 10–100 eV (Chaston et al., 2015; Gkioulidou et al., 2019; Hull et al., 2019; Kistler et al., 2016; Nosé et al., 2016, 2018, 2021). Using the Van Allen Probes data, Nosé et al. (2016) first performed a statistical study of the unidirectional energy-dispersed O^+ flux. They revealed that the unidirectional energy-dispersed O^+ flux accompanies 80% of the selected dipolarization events and that its direction is parallel (antiparallel) to the magnetic field when the satellites are in the southern (northern) hemisphere. The similar features in the direction of low-energy O^+ flux enhancements were also observed by the Arase satellite in the more inner magnetosphere and at higher geomagnetic latitudes, although the occurrence probability was 36% (Nosé et al., 2021). These results suggest that ionospheric O^+ ions flow out from the upper ionosphere at the onset of substorms, move along the magnetic field, and arrive at satellites to be identified as the flux enhancement of the field-aligned low-energy O^+ ion (FALEO). If the outflow is initiated simultaneously over the energy range of 10 eV to ~1 keV, FALEO is observed with the energy-dispersion signature, owing to the time-of-flight effect of ions traveling at different speeds from the upper ionosphere to the satellites. FALEOs travel toward the geomagnetic equator, where they may experience pitch angle scattering, and thereby remain bouncing between both hemispheres. It is possible that they drift eastward because of their low energy (<1 keV) and contribute to the O^+ content of the inner magnetospheric plasma, resulting in the change in the ion composition or the ion mass density. These parameters have an impact on numerous phenomena in the magnetosphere, such as solar-wind/magnetosphere coupling, magnetotail reconnection and substorms, Kelvin-Helmholtz instabilities on the

Software: M. Nosé, A. Matsuoka, Y. Miyoshi, K. Asamura, T. Hori, M. Teramoto
Validation: M. Nosé
Visualization: M. Nosé
Writing – original draft: M. Nosé
Writing – review & editing: M. Nosé, Y. Miyoshi, T. Hori, M. Hirahara

magnetopause, electromagnetic-ion-cyclotron and ultralow-frequency wave-particle interactions, aurora structuring, and spacecraft charging (Delzanno et al., 2021). Thus, the study of FALEO provides an important key to comprehensive understanding of these phenomena.

Gkioulidou et al. (2019) investigated the spatial extent and temporal evolution of the unidirectional O^+ outflow event that was simultaneously identified by the Van Allen Probes A and B satellites. Probe A moved ahead of Probe B approximately 1 hr along the same orbit in the northern hemisphere. They found that the unidirectional O^+ outflow occurs over a limited duration in time but extended L range ($L \sim 3.0$–5.5). In the present study, we examine flux enhancements of FALEO simultaneously observed by the Arase, Van Allen Probes A and B satellites on 22 September 2018. The three satellites were located in the nightside inner magnetosphere (Arase at magnetic local time (MLT) = 0.3 hr, $L = 6.2$, geomagnetic latitude (GMLAT) = −9.6°; Probe A at MLT = 0.7 hr, $L = 5.5$, GMLAT = 14.7°; Probe B at MLT = 0.0 hr, $L = 5.3$, GMLAT = 10.6°) at a substorm onset. To our knowledge, this is the first report of simultaneous observations of FALEO by three satellites located in both hemispheres. The rest of the paper is organized as follows. Section 2 introduces ground signatures of a substorm occurring at 05:24 UT on 22 September 2018 and describes in detail the FALEO event that appears after the substorm onset. Arase observes FALEO only in the parallel direction to the magnetic field in the energy range from a few keV to 100 eV. Probes A and B, however, identify FALEO in both parallel and antiparallel directions over a few keV to 10 eV. The antiparallel fluxes appear slightly earlier than the parallel fluxes. Multiband flux structure of the FALEO is clearly observed by Probes A and B. In Section 3, we perform numerical calculations of test O^+ ion trajectories and create energy-time spectrograms observed by three virtual satellites, which have the same orbits as Arase, Probes A and B. The motion of the test O^+ ions is traced for 10 hr and their spatial distribution in the inner magnetosphere is examined. Section 4 compares the energy-time spectrograms between the real satellites and the virtual satellites, and discusses the contribution of FALEO to the O^+ content of the inner magnetospheric background plasma, in terms of the formation of the warm plasma cloak or the oxygen torus. The conclusions are given in Section 5.

2. Observations

2.1. Geomagnetic Indices and Geomagnetic Field Observations

Figure 1a displays the SYM-H index (Iyemori et al., 1992) for 21–25 September 2018. A geomagnetic storm starts with an increase of the SYM-H index (i.e., sudden commencement) at ∼15:00 UT on September 21, develops until SYM-H reaches a minimum value of −49 nT at 07:36–07:49 UT on September 22, and decays gradually in 3–4 days. The time interval of interest in this study is 05:00–07:00 UT on September 22, which is indicated with a horizontal red bar. This time interval is just before the peak of the magnetic storm and the SYM-H index is about −35 nT.

Figure 1b shows the Wp index for 05:00–07:00 UT on 22 September 2018. This index is invented to measure the wave power of low-latitude Pi2 pulsations (Nosé et al., 2012; World Data Center for Geomagnetism, Kyoto, et al., 2016). Figure 1c gives the SML index for the same 2-hr time interval. The SML index is derived from the magnetometer data provided by the SuperMAG collaborators to best represent the maximum westward auroral electrojets strength in the northern hemisphere (Gjerloev, 2012; Newell & Gjerloev, 2011a, 2011b). As marked with a vertical dotted magenta line, at 05:24 UT, the Wp index starts to increase and the SML index starts to decrease. These variations indicate that a substorm starts developing from 05:24 UT. Both the Wp index and the SML index reach the peak values within 10 min after the onset, indicating that the substorm development has ceased by 05:34 UT.

Figure 2 displays magnetic field variations for 05:00–07:00 UT on 22 September 2018 measured at 17 observatories that collaborate with SuperMAG. In each panel, the name of the observatory and its operator are shown in the top-left corner. The magnetic field variations are shown in *NEZ* coordinates, where N is positive in the direction of local magnetic north (red curve), E is positive in the local magnetic east direction (blue curve), and Z is positive vertically down (green curve). GMLAT and MLT at 05:24 UT (i.e., substorm onset) of the observatory are indicated in the bottom-right corner. Observatories at almost the same MLT are grouped in the same column; from left to right columns, MLT ∼ 21.2 hr, ∼23.0 hr, ∼0.7 hr, and ∼1.7 hr. In each column, panels are sorted from high to low latitudes (GMLAT = ∼69° to ∼58°).

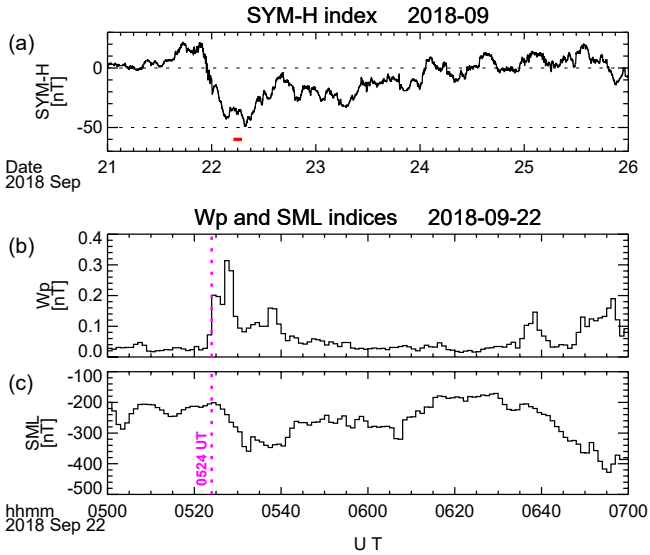

Figure 1. (a) The SYM-H index for September 21–25, 2018. A horizontal magenta bar indicates the time interval of interest in this study, that is, 05:00–07:00 UT on September 22. (b, c) The Wp and SML indices for 05:00–07:00 UT on September 22. Substorm onset is identified at 05:24 UT as indicated with a vertical dotted magenta line.

At 05:24 UT, magnetic field in the *N* component (red) starts to decrease at observatories of GMLAT > 63° with the largest magnitude at Island Lake and Gillam, indicating development of westward electrojets. The *E* component (blue) after 05:24 UT shows no significant changes at ~21.2 MLT, but it increases at ~23.0 MLT (Gillam, Island Lake, and Brandon) and decreases at ~0.7 MLT and ~1.7 MLT. This is due to a region 1 type field-aligned current (i.e., substorm wedge current) centered between ~23.0 MLT and ~0.7 MLT. The *Z* component (green) after 05:24 UT changes the polarity of variations between Gillam and Island Lake at ~23.0 MLT and between Radisson and Kapuskasing at ~0.7 MLT. This can be interpreted as the development of the westward electrojet with a peak located between these latitudinally separated stations, that is, between 66.16° GMLAT and 63.70° GMLAT at ~23.0 MLT and between 63.54° GMLAT and 59.51° GMLAT at ~0.7 MLT. Assuming that the peak latitude of the westward electrojet does not strongly depend on MLT, we suppose the peak around 63.6° GMLAT. To summarize, the substorm is considered to start around GMLAT = 63.6° (*L* = 5.06) and premidnight (between 23.0 and 0.7 hr MLT).

2.2. Locations of Arase, Van Allen Probe A, and Van Allen Probe B

Figures 3a and 3b show the orbital segments of Arase (green curve), Van Allen Probe A (red curve), and Van Allen Probe B (blue curve) during 05:00–07:00 UT on 22 September 2018 in the *L*-MLT plane and the meridional plane, respectively (Mauk et al., 2013; Miyoshi, Shinohara, & Jun, 2018;

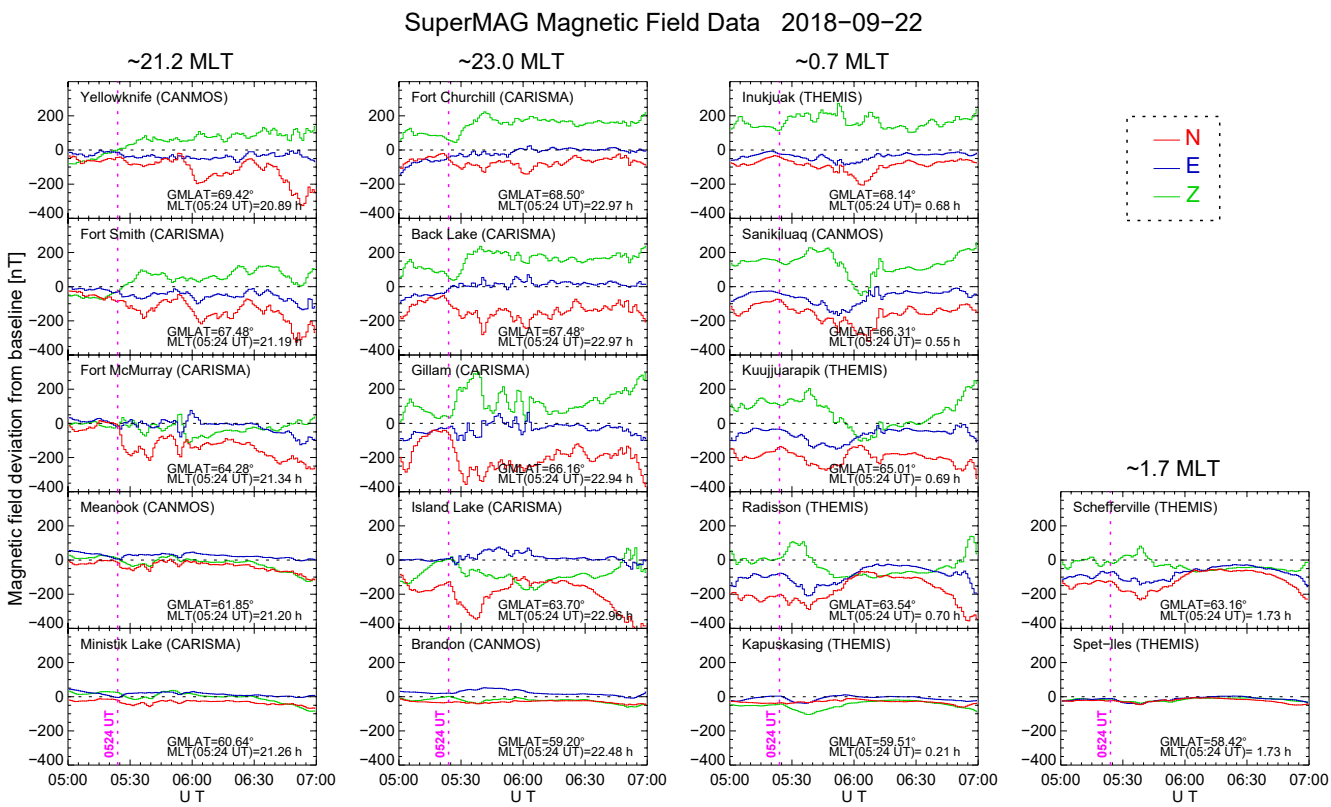

Figure 2. Magnetic field variations in *NEZ* coordinates for 05:00–07:00 UT on September 22, 2018 measured at 17 observatories that collaborate with SuperMAG. In each panel, names of the observatory and its operator are shown in the top-left corner, and GMLAT and MLT at 05:24 UT of the observatory are indicated in the bottom-right corner. Vertical dotted magenta lines are drawn at 05:24 UT.

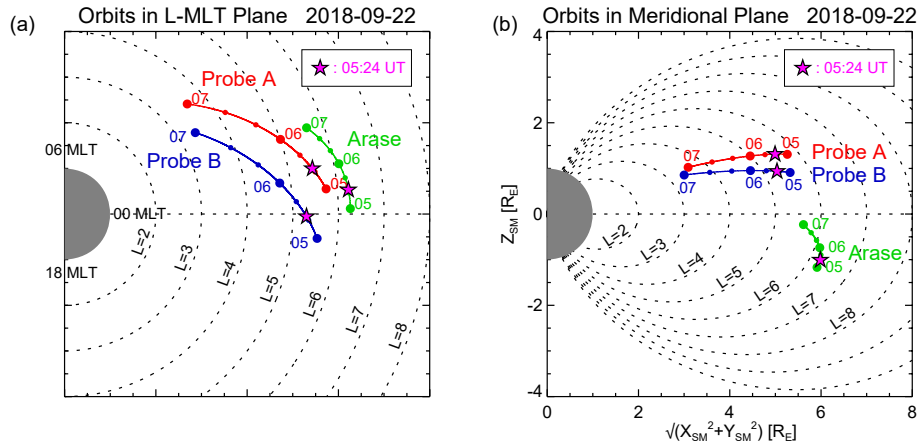

Figure 3. (a) Orbital segments of Arase (green), Van Allen Probe A (red), and Van Allen Probe B (blue) during 05:00–07:00 UT on September 22, 2018 in the *L*-MLT plane. Dots on the orbits show the locations of the satellites every 20 min with larger dots at integer hours. Magenta starts indicate the locations of the satellites at substorm onset (i.e., 05:24 UT). (b) Same as Figure 3a but in the meridional plane.

Miyoshi, Shinohara, Takashima, et al., 2018), where *L* values are defined in the dipole field. Dots on the orbits delineate the locations of the satellites every 20 min with larger dots at integer hours. Magenta stars indicate the locations of the satellites at substorm onset (i.e., 05:24 UT).

All three satellites are flying along inbound paths: Arase moves from $L = 6.3$ to $L = 5.6$, while Probes A and B traverse the more inner magnetosphere from $L = 5.8$ to $L = 3.4$. From Figure 3a, we see that they are located near midnight (23.6–0.4 hr MLT) at 05:00 UT and move to the postmidnight sector (1.3–2.8 hr MLT) at 07:00 UT. At substorm onset, their locations are (*L*, MLT) = (6.2, 0.3 hr) for Arase, (5.5, 0.7 hr) for Probe A, and (5.3, 0.0 hr) for Probe B. The ground observations (Figure 2) suggest that the substorm onset is located around 63.6° GMLAT ($L \sim 5.06$) and between ~23.0 MLT and ~0.7 MLT, which is the closest to Probe B. It is noted from Figure 2b that Arase is flying below the geomagnetic equator (GMLAT = −11.2° to −2.4°), while Probes A and B are located above the geomagnetic equator (GMLAT = −9.7° to −18.3°).

2.3. Arase Observation

Figure 4 compiles observations by Arase for 05:00–07:00 UT on 22 September, 2018. From top to bottom, presented are the magnetic field deviation (ΔV, ΔD, and ΔH) measured by the fluxgate magnetometer (MGF; Matsuoka, Teramoto, Imajo, et al., 2018; Matsuoka, Teramoto, Nomura, et al., 2018) and the energy-time spectrograms of H^+ and O^+ ions in three different pitch angle ranges (α = 0–30°, 75–105°, and 150–180°) measured by the low-energy particle experiments-ion mass analyzer (LEPi; Asamura, Kazama, et al., 2018; Asamura, Miyoshi, & Shinohara, 2018). The magnetic field deviation is defined as a difference of the measured magnetic field from the sum of the International Geomagnetic Reference Field (IGRF)-13 internal model field (Alken et al., 2021) and the Tsyganenko T89 external model field (Tsyganenko, 1989) with Kp = 0 (Matzka, Bronkalla, et al., 2021; Matzka, Stolle, et al., 2021). It is expressed in *VDH* coordinates, where *H* is antiparallel to the Earth's dipole axis, *D* is perpendicular to the radius vector and *H*, and points toward east, and *V* completes a right-handed orthogonal system in that order. The cadence of the magnetic field data shown in Figure 4a is the satellite spin period (~8 s). LEPi has ~4π sr spatial coverage by using the spin motion of the satellite and samples ions with mass discrimination in the energy range of 0.01–25 keV/q with 32 logarithmically spaced energy steps when operated in the normal mode. Because of limitation of the telemetry during this event, we obtained one complete energy spectrum with the full angular coverage for ~8 s every four satellite revolutions (i.e., ~32 s). In Figures 4b–4g, we display the LEPi data with a time resolution of ~32 s.

In Figure 4a, we find that the magnetic field shows no clear changes at ground substorm onset (05:24 UT, the first vertical magenta line) but suddenly changes at 05:27 UT (the second vertical magenta line) with an increase of ΔH and a decrease of $|\Delta V|$. This is a typical signature of magnetic field dipolarization in the inner magnetosphere, that is, configuration change from a stretched magnetic field to a more dipolar-like magnetic field (e.g.,

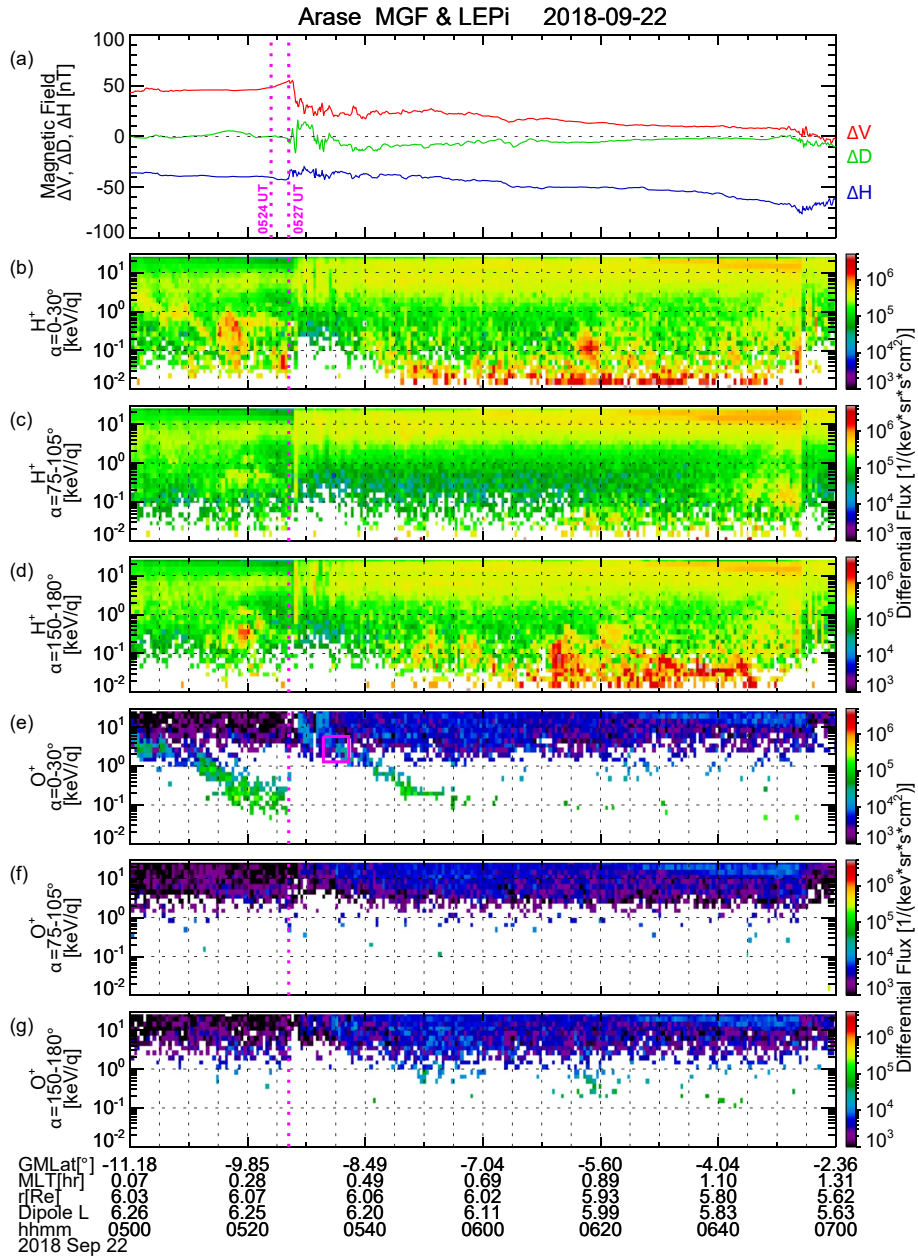

Figure 4. Magnetic field and ion flux measurements by Arase for 05:00–07:00 UT on September 22, 2018. From top to bottom, displayed are (a) the magnetic field deviation from the model field in *VDH* coordinates (ΔV, ΔD, and ΔH), (b–d) the energy-time spectrograms of H^+ at different pitch angles of α = 0–30°, 75–105°, and 150–180°, and (e–g) the energy-time spectrograms of O^+ at different pitch angles of α = 0–30°, 75–105°, and 150–180°. In Figure 4a, two vertical magenta lines represent times of the ground substorm onset (05:24 UT) and magnetic field dipolarization (05:27 UT). In Figures 4b–4g, vertical magenta lines are drawn at 05:27 UT. A magenta square indicates time and energy where the energy-dispersed O^+ flux enhancement stars.

Nagai, 1991; Nagai et al., 1996). Three-minutes delay from the ground substorm onset can be interpreted in terms of a propagation time of the dipolarization region in the inner magnetosphere.

In association with the dipolarization at 05:27 UT, the H^+ fluxes are enhanced almost simultaneously over the energy range of ~1–25 keV (Figures 4b–4d). This is consistent with results of previous studies that ions are locally accelerated to higher than 1–30 keV during dipolarization (Birn et al., 1997, 1998; Mauk, 1986; Möbius et al., 1987; Sánchez et al., 1993). However, the dipolarization seems to cause no significant flux enhancements in

the lower energy range (<1 keV). Although there are H^+ flux increases in the field-aligned directions ($\alpha = 0$–$30°$ and 150–180°) at 10–100 eV from 05:45 UT to 06:50 UT (reddish colors), we think that they are due to the effect of satellite orbital motion into lower L shells. This is because the warm (>30 eV) H^+ density or the 100 eV H^+ flux has an inward gradient with a peak around L = 3–4 during geomagnetically active times (Fernandes et al., 2017; Jahn et al., 2017) and H^+ flux at ≤500 eV shows a cigar-type pitch angle distribution in the magnetosphere on the nightside (Wang et al., 2013). Similarly, the O^+ fluxes also show enhancements in the energy range of a few keV to 25 keV just after the dipolarization (Figures 4e–4g), which are caused by local acceleration. However, as seen in Figure 4e, approximately 5 min later, the energy-dispersed O^+ flux enhancement appears in a direction parallel to the magnetic field (α = 0–30°). This energy-dispersion signature seems to start from a few keV around 05:35 UT, as indicated with a magenta square, and continues through 100 eV around 06:00 UT, which is referred as FALEO in this study. On the other hand, no low-energy O^+ flux enhancements are seen at α = 75–105° and 150–180° (Figures 4f and 4g). These features are consistent with those of O^+ ions that have been reported by previous studies (Chaston et al., 2015; Gkioulidou et al., 2019; Hull et al., 2019; Kistler et al., 2016; Nosé et al., 2016, 2018, 2021).

We note the very similar energy-dispersed O^+ flux enhancement at α = 0–30° during 05:00–05:27 UT, which is considered to be also FALEO. This event is related to a substorm onset at 04:52 UT (not shown here). In the present study, however, we do not further examine this FALEO event, because no corresponding O^+ flux enhancements are clearly found by Probe A and Probe B as shown later. Interested readers can refer to Supporting Information S1, where figures and discussion for this FALEO event are given.

2.4. Van Allen Probe A Observation

Figure 5 displays observations by Van Allen Probe A for the identical 2-hr time interval in the same format as Figure 4, except that the magnetic field deviation is measured by the Electric and Magnetic Field Instrument Suite and Integrated Science (EMFISIS) instrumentation suite (Kletzing et al., 2013) and the H^+ and O^+ ion fluxes are measure by the Helium, Oxygen, Proton, and Electron (HOPE) mass spectrometer (Funsten et al., 2013), which is one of the three instruments of the Energetic Particle, Composition, and Thermal Plasma (ECT) suite (Spence et al., 2013). The temporal resolution of the EMFISIS data shown in Figure 5a is 1 s. The ECT-HOPE instrument covers an energy range from 0.001 to 50 keV that is scanned by 72 logarithmically spaced energy steps. Its spatial coverage is ∼4π sr and one complete omnidirectional spectrum of each ion species can be obtained every two spin periods (∼22 s). In Figures 5b–5g, however, we display the ion flux data averaged over ∼44 s in the energy range of 0.01–25 keV, for better statistical significance and for easy comparison with the Arase/LEPi data.

The magnetic field has no clear changes at ground substorm onset (05:24 UT) and starts to increase in ΔH and decrease in $|\Delta V|$ at 05:27 UT (Figure 5a), indicating dipolarization. There is 3 min delay between the ground substorm onset and the dipolarization, which is again interpreted as the propagation time of the dipolarization region in the inner magnetosphere.

The H^+ fluxes shown in Figures 5b–5d are enhanced in the energy range of ∼1–25 keV at 05:27 UT. We suppose that the enhancement is caused by local ion acceleration in association with the dipolarization. After ∼05:50 UT, there are large flux increases at low energies of < a few hundreds of eV (reddish colors), which would be caused by satellite orbital motion into the more inner magnetosphere. These features of the H^+ fluxes are very similar to those observed by Arase (Figures 4b–4d). In Figures 5e–5g, the O^+ fluxes around 10 keV are increased at 05:27 UT, but the most distinct enhancements in the O^+ fluxes are those with the energy-dispersion signature from a few keV down to 10 eV in both parallel (α = 0–27°) and antiparallel (α = 153–180°) directions, that is FALEO. As indicated with magenta squares, the parallel flux enhancement starts around 05:45 UT at ∼1 keV (Figure 5e) and the antiparallel flux enhancement appears slightly earlier around 05:40 UT at a few keV (Figure 5g). These enhancements of FALEO repeat 2–3 times to form a multiband structure.

2.5. Van Allen Probe B Observation

The magnetic field and ion flux data from Van Allen Probe B are displayed in Figure 6 in the same format as Figure 5. These data are obtained by the EMFISIS and ECT-HOPE instruments, which are identical to those onboard Probe A. The magnetic field starts to gradually change at ground substorm onset (05:24 UT), and then shows strong disturbances at 05:27 UT with an increase of ΔH and a decrease of $|\Delta V|$. The first gradual change,

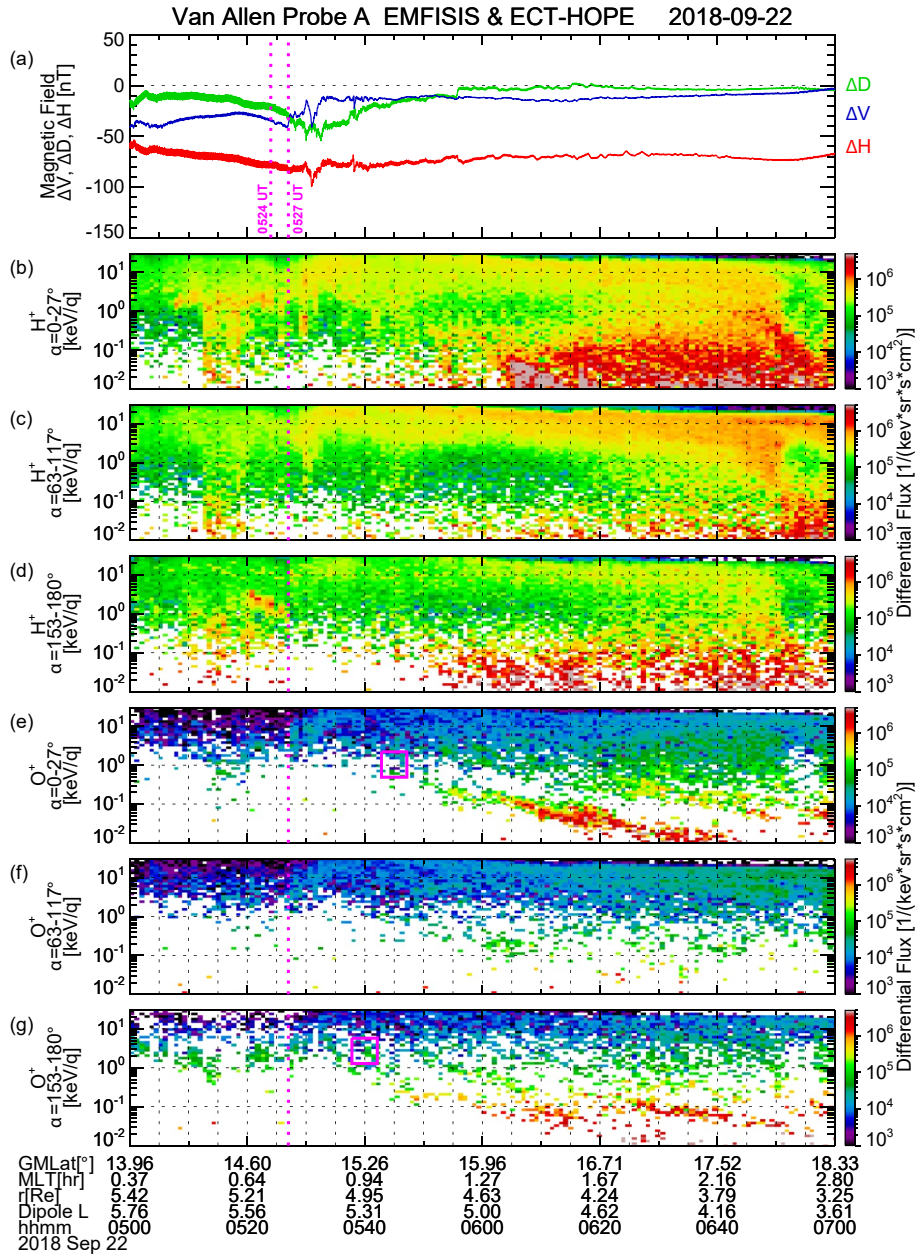

Figure 5. Same as Figure 4 but for Van Allen Probe A. The energy-time spectrograms are shown for different pitch angles of $\alpha = 0$–$27°$, 63–117°, and 153–180°.

which was not clearly identified by Arase and Probe A, may be detected because Probe B is located closer to the onset region than the other two. The 3-min delay is considered to be a propagation time of the dipolarization region.

It does not seem that the dipolarization causes significant flux changes in H^+ (Figures 6b–6d). There are overall flux increases in the low energy below 100 eV after 05:50 UT, because Probe B moves into the more inner magnetosphere. On the other hand, the O^+ flux again shows a striking flux change, that is, the energy-dispersed flux enhancement from a few keV to 10 eV in both parallel ($\alpha = 0$–$27°$) and antiparallel ($\alpha = 153$–$180°$) directions, indicating that Probe B also observes FALEO. It appears to start within ~5 min after the dipolarization. The parallel flux begins around 05:32 UT at a few keV (Figure 6e) and the antiparallel flux appears almost simultaneously

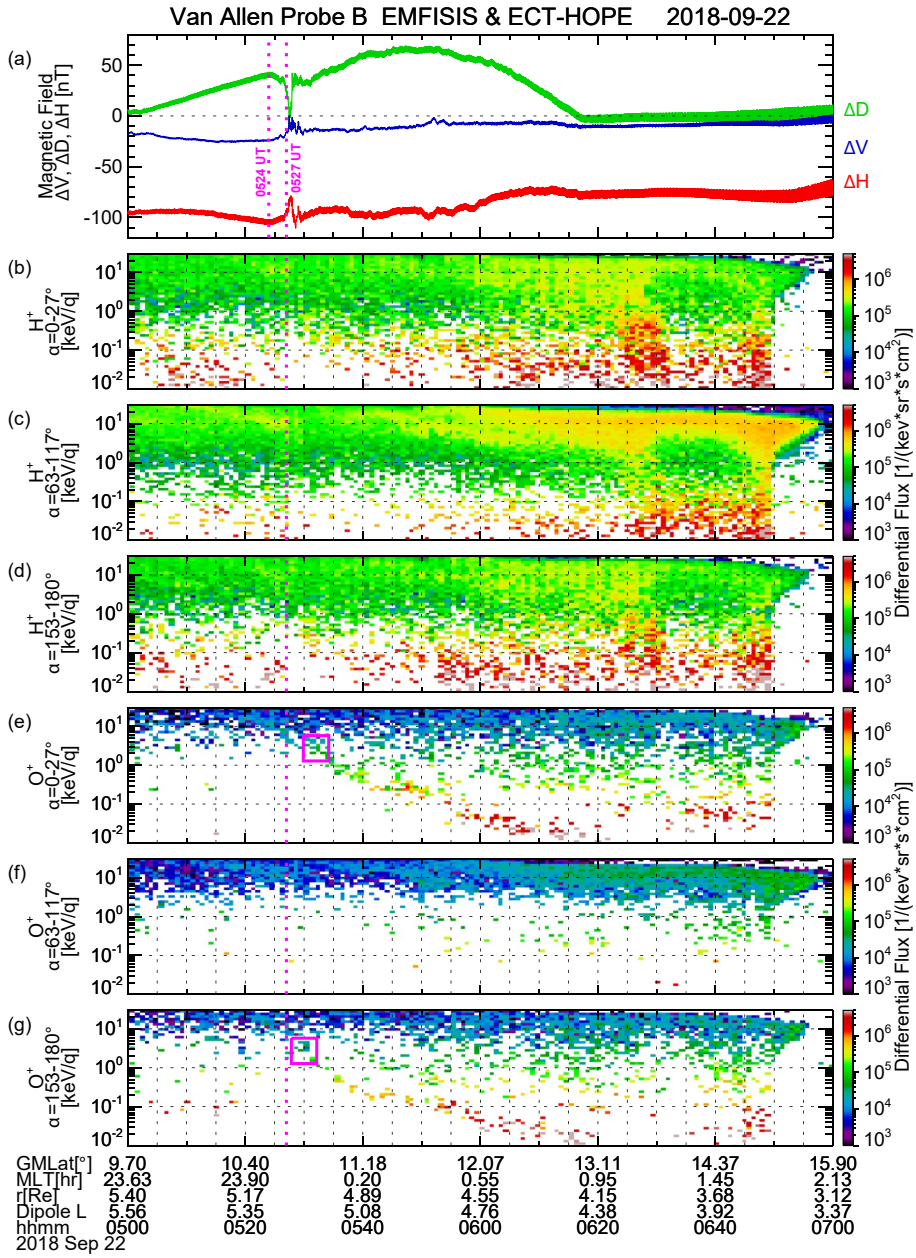

Figure 6. Same as Figure 5 but for Van Allen Probe B.

or slightly earlier (around 05:30 UT) at a few keV (Figure 6g), as highlighted with magenta squares. We also find a multiband structure of FALEO, although it is not so clear as seen in the Probe A observations.

2.6. Summary of Satellite Observations

For a detailed inspection of the temporal evolution of FALEO, the energy-time spectrograms of O^+ ions observed by Arase, Probe A, and Probe B are stacked in Figure 7. The displayed data are identical to those of Figures 4e–4g, 5e–5g, and 6e–6g. Dipolarization is simultaneously identified at 05:27 UT by all of three satellites, which is indicated with vertical dotted magenta lines. Then, it seems that FALEO is first observed by Probe B within ∼5 min after the dipolarization. Hereafter we define the start time of FALEO to be the time of a flux enhancement at 1 keV, which is delineated with a horizontal dotted magenta line in each panel. The start time of FALEO at Probe B is ∼05:33 UT for the antiparallel direction and ∼05:35 UT for the parallel direction, as

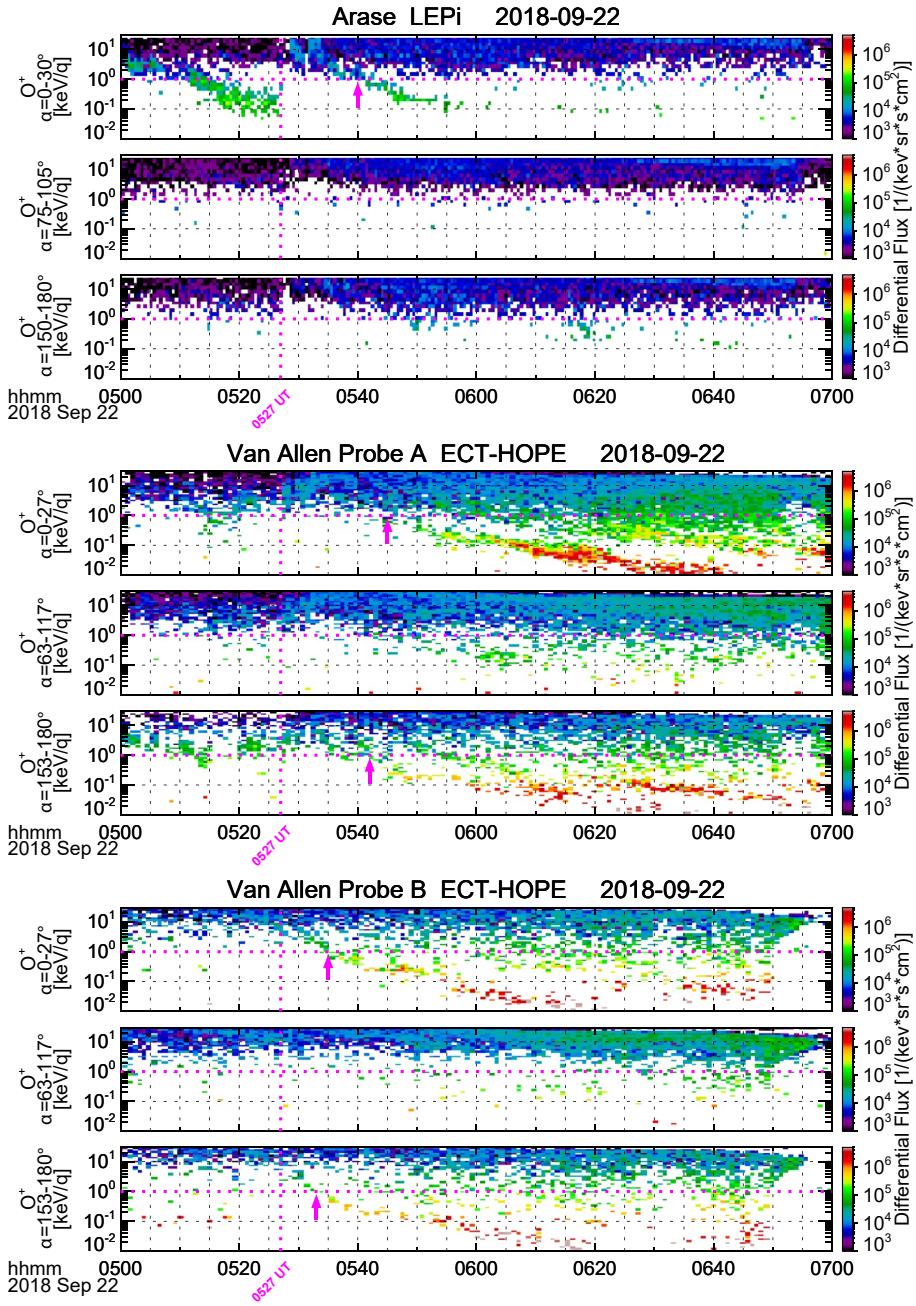

Figure 7. Summary plots of the energy-time spectrograms of O^+ ions measured by Arase, Probe A, and Probe B. Data are the same as those of Figures 4e–4g, 5e–5g, and 6e–6g. Magenta arrows indicate the time of appearance of FALEO, which is defined as the time of a flux enhancement at 1 keV (a horizontal dotted magenta line).

indicated with magenta arrows. Occurrence of FALEO follows at Arase around 05:40 UT in only the parallel direction. Finally, Probe A detects FALEO at ∼05:42 UT in the antiparallel direction and at ∼05:45 UT in the parallel direction. It should be noted that FALEO at Arase disappears at ∼100 eV around 06:00 UT, while it continues for ∼1 hr at Probes A and B and has a multiband structure.

It is likely that FALEO originates from the ion outflow from the upper ionosphere at substorm onset. We therefore expect that the earliest appearance of FALEO at Probe B is due to that the substorm onset region is closest to Probe B, which is consistent with the brief statement in Section 2.2 (or see Figures 2 and 3). The antiparallel flux starts earlier than the parallel flux at both Probes A and B. This can be attributed to the location of both satellites

Table 1
Initial Parameters of Test O^+ Ions

Parameter	Value	Interval
Release area (L)	5.0–5.4	$\Delta L = 0.02$
(MLT)	23.0–0.6 hr	ΔMLT = 0.2 hr
Release altitude	4,000 km	
Initial energy	10 eV–1 keV	$\Delta E = 10^{0.1}$
Hemispheres	Northern/Southern	
Initial pitch angle	100°(N)/80°(S)	
t_{delay} after 05:24 UT	$10 \times \lvert\text{MLT} - 23.8\ \text{hr}\rvert + 10 \times (L - 5.0) + 3$ min	

above the geomagnetic equator; they observe O^+ ions just outflowing from the northern ionosphere ($\alpha > 90°$) earlier than those from the southern ionosphere ($\alpha < 90°$). Since Arase is located below the geomagnetic equator, the opposite is expected, but there is no FALEO in the antiparallel direction. We think that FALEOs outflowing from the northern hemisphere ($\alpha < 90°$) are convected into the inner magnetosphere on the way to the Arase location and thus does not reach Arase. This can happen in larger L shell at the Arase location, where the magnitude of the magnetic field is smaller and the $E \times B$ drift velocity becomes larger. This mechanism can also explain the lower cutoff energy of ~100 eV for FALEO in the parallel direction: it takes longer time for low-energy O^+ ions (<100 eV) to travel from the southern ionosphere to the Arase location than high energy O^+ ions (>100 eV), during which they drift into the more inner magnetosphere so that they leave the field line threading Arase.

3. Numerical Simulations for Trajectories of FALEO

3.1. Simulation Setup

We perform numerical calculations of O^+ ion trajectories to compare with the satellite observations and to investigate the destination of FALEOs. The ion trajectories are computed by integration of the guiding center equations of motion with the simulation code developed by Delcourt et al. (1990), in which the Tsyganenko T89 external model (Tsyganenko, 1989) field and the Volland-Stern convection electric model field (Maynard & Chen, 1975; Stern, 1975; Volland, 1973) are used. The model fields are given for Kp = 4, because the Kp values of 03–06 UT and 06–09 UT on 22 September 2018 are 4+ and 4− (Matzka, Bronkalla, et al., 2021; Matzka, Stolle, et al., 2021).

Initial parameters of test O^+ ions to be traced are summarized in Table 1. The test O^+ ions are released from grid points (L_i, MLT_j) in the area of L = 5.0–5.4 by MLT = 23.0–0.6 hr above the northern ionosphere at altitude of 4,000 km with the initial pitch angle of $\alpha = 100°$. Here, L_i is the ith step of the 21 equally spaced L steps (i.e., $L_1 = 5.0$, $L_{21} = 5.4$, and $\Delta L = L_{i+1} - L_i = 0.02$), and MLT_j is the jth step of the nine equally spaced MLT steps (i.e., $\text{MLT}_1 = 23.0$ hr, $\text{MLT}_9 = 0.6$ hr, and $\Delta\text{MLT} = \text{MLT}_{j+1} - \text{MLT}_j = 0.2$ hr). This source area is determined by referring to the ground observations of the magnetic field disturbances shown in Figure 2, in spite of their sparse distribution. It was found from Figure 2 that the substorm started around GMLAT = 63.6° (L = 5.06) and between MLT = 23.0 and 0.7 hr. We postulate that the latitudinal width of the source area is 1°, resulting in the poleward boundary of GMLAT = 64.6° (L = 5.44). The altitude of 4,000 km and the initial pitch angle of $\alpha = 100°$ are based on the idea that ionospheric O^+ ions are uplifted by soft electron precipitation and/or Poynting flux enhancement at substorm onset and then they are further accelerated by electromagnetic disturbances in the perpendicular direction to flow out from the upper ionosphere (e.g., Chaston et al., 2004, 2005; Hull et al., 2020; Shen & Knudsen, 2020; Strangeway et al., 2000, 2005). The test O^+ ions are set to have an initial energy E_k between 10 eV and 1 keV, where E_k is the kth step of the 21 logarithmically equally spaced energy steps (i.e., $E_1 = 10^1$ eV, $E_{21} = 10^3$ eV, and $\Delta E = E_{k+1}/E_k = 10^{0.1}$). We assume that the westward electrojet starts to develop at (L, MLT) = (5.0, 23.8 hr) at 05:24 UT and expands both poleward and longitudinally with the speed of 10 min/L and 10 min/MLT. We also assume that ionospheric O^+ needs 3 min to outflow after the energy input to the ionosphere due to disturbances. This time delay is considered reasonable because Fuselier et al. (2002) and Khan et al. (2003) showed that ion outflow responds to the solar-wind dynamic pressure promptly (<2 min); Nosé et al. (2009) found that ion outflow is delayed by several minutes from storm time substorms; and Ogawa

et al. (2013) reported that ion upflow occurs about 6 min after the auroral initial brightening. From these assumptions, the test O^+ ions are released at t_{delay} after 05:24 UT, where t_{delay} is expressed as

$$t_{delay}\,[\mathrm{min}] = 10\,[\mathrm{min/hr}] \times |\mathrm{MLT}_j\,[\mathrm{hr}] - 23.8\,[\mathrm{hr}]| + 10\,[\mathrm{min}/L] \times (L_i - 5.0) + 3\,[\mathrm{min}].$$

Therefore, t_{delay} ranges from 3 min at (L, MLT) = (5.0, 23.8 hr) to 15 min at (L, MLT) = (5.4, 23.0 hr) and (5.4, 0.6 hr), indicating that the release time of O^+ ions is between 05:27 UT and 05:39 UT. Test O^+ ions are also released from above the southern ionosphere with the identical parameters except for $\alpha = 80°$. Thus, the total number of the test O^+ ions in the simulation space is 21 (L) × 9 (MLT) × 21 (E) × 2 (hemispheres) = 7,938. In the same way as Nosé et al. (2021), we include an effect of pitch angle scattering near the geomagnetic equatorial plane ($|Z_{SM}| \leq 0.5\ R_E$), where α is changed toward toward 90° at the rate of $5°/R_E$ only in the first equatorial crossing. (We surmise that the pitch angle scattering near the geomagnetic equator is caused by strong magnetic field fluctuations during the magnetic field dipolarization or a small curvature radius of the stretched magnetic field.) The computation of the O^+ ion trajectories is performed until the travel time of an O^+ ion reaches 10 hr or its altitude is less than 300 km (i.e., being lost in the ionosphere).

3.2. Energy-Time Spectrograms Observed by Virtual Satellites

We fly virtual satellites in the numerical simulation space and create energy-time spectrograms observed by them for comparison with the real observations. The virtual satellites follow the identical orbits as the real satellites. If a relative distance between a test O^+ ion and a virtual satellite is less than 0.5 in L, 0.5 hr in MLT, and 1.0° in GMLAT, we consider that the O^+ ion is observed by the virtual satellite. Every minute from 05:27 UT (start of O^+ ions) to 07:00 UT, we check if test O^+ ions are observed by three virtual satellites, that is, virtual Arase, virtual Probe A, and virtual Probe B. When observed, according to the pitch angle, the test O^+ ions are classified into four categories: parallel ($\alpha = 0$–30°), perpendicular ($\alpha = 75$–105°), antiparallel ($\alpha = 150$–180°), and others. Then, in each category, the number of the observed O^+ ions is counted in the logarithmically equally spaced energy bins from 10 eV to 50 keV ($\Delta E = 10^{0.1}$). Finally, the number of O^+ ions is divided by the center energy of the energy bin to convert into "pseudo flux." This is for an easier comparison with the satellite observations (Figure 7), in which data are given in differential flux (J). (Note that J is calculated by $J = gC/E$, where C is the detected ion counts, E is the center energy of the energy channel, and g is an instrument specific constant).

Figure 8 shows the results of the energy-time spectrograms observed by the virtual satellites. The plot format follows that of Figure 7; from top to bottom, displayed are the energy-time spectrograms of O^+ ions in the directions parallel, perpendicular, and antiparallel to the magnetic field for virtual Arase, those for virtual Probe A, and those for virtual Probe B. In each panel, the total flux calculated by integrating the pseudo flux over the entire time and energy range is indicated. Virtual Arase observes O^+ fluxes in both the parallel and antiparallel directions, but the total flux in the parallel direction is more than 3.2 times larger than that in the antiparallel direction, indicating the dominance of the parallel flux. The parallel flux has the energy-dispersion signature from 1 keV to ∼100 eV. The start time of the parallel flux has a wide range from 05:35 UT to 05:45 UT, resulting in a thick band structure. The antiparallel flux starts between 05:38 UT and 05:46 UT. Virtual Probe A detects clear O^+ flux enhancements in both the parallel and antiparallel directions with the energy-dispersion signature from 1 keV to 10 eV. The flux enhancements start earlier in the antiparallel flux around 05:37–05:42 UT than in the parallel flux around 05:43–05:47 UT. The energy-dispersion signature repeats 2–3 times and the multiband structure is established. Virtual Probe B indicates the almost similar signature as virtual Probe A, but the energy-dispersed flux enhancements appear 4–8 min earlier than Probe A. The antiparallel flux starts around 05:32–05:38 UT and the parallel flux starts around 05:35–05:40 UT. The multiband structure of the flux enhancement is identified. In all three virtual satellites, the perpendicular flux ($\alpha = 75°$–105°) is detected only near 1–2 keV, and its total flux is much smaller than those of the parallel and antiparallel fluxes.

3.3. Trajectory of FALEO From Above Ionosphere to Virtual Satellites

In Figure 8, virtual Arase observes FALEOs predominantly in the parallel direction with the energy-dispersion signature down to ∼100 eV, while both virtual Probe A and Probe B detect FALEOs in both the parallel and antiparallel directions with the energy-dispersion signature extending to ∼10 eV. These differences in the energy-time spectrograms between satellites can be well understood from trajectories of test O^+ ions in the meridional

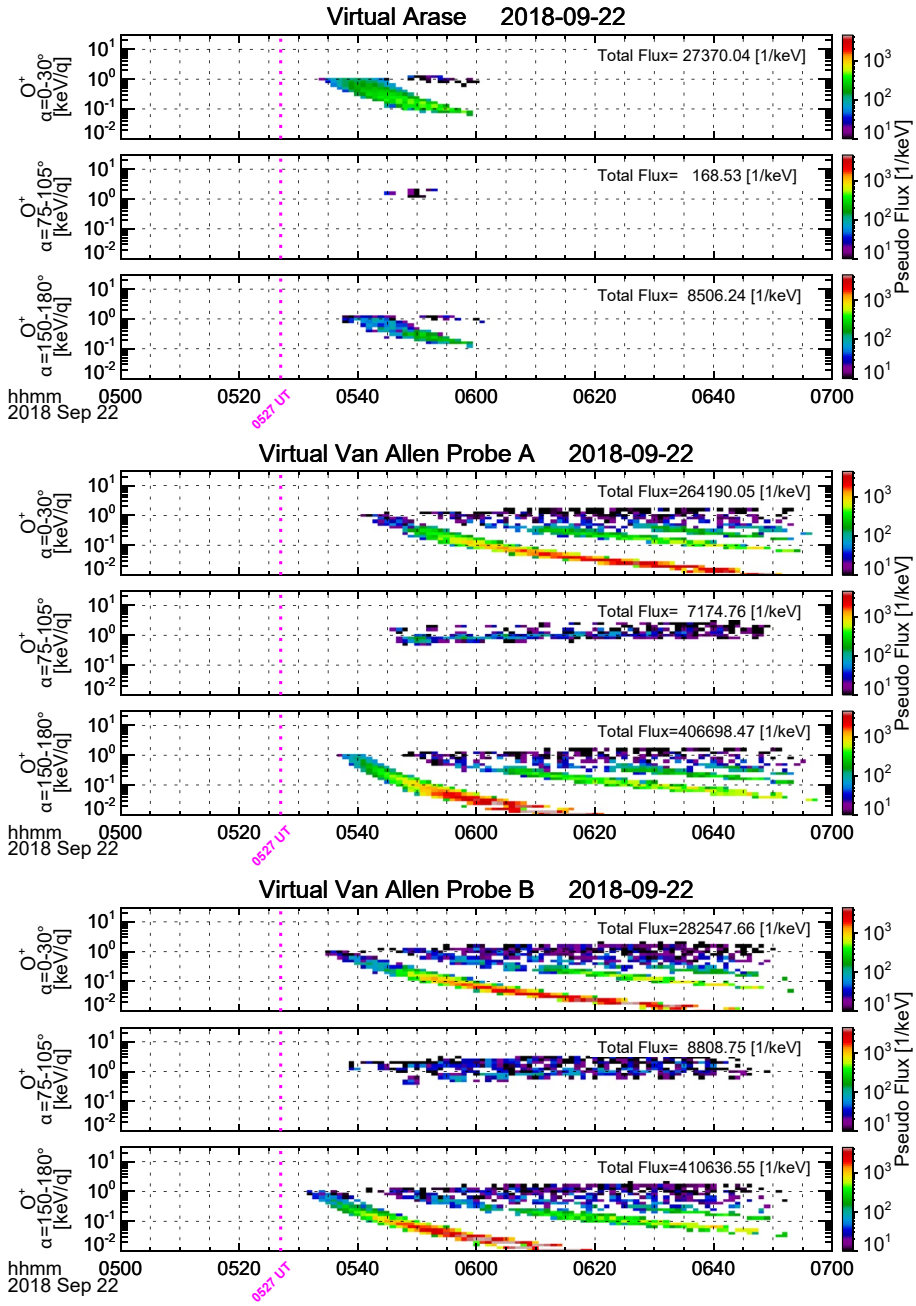

Figure 8. The energy-time spectrograms observed by virtual satellites (virtual Arase, virtual Probe A, and virtual Probe B) flying in the numerical simulation space. In the numerical simulation, test O^+ ions are released from the upper ionosphere at $L = 5.0–5.4$ and MLT = 23.0–0.6 hr in both hemispheres, and their trajectories are calculated. The format follows that of Figure 7. The total flux value calculated by integrating the pseudo flux over the entire time and energy range is indicated in the upper-right corner of each panel.

plane before 07:00 UT, which are displayed in Figure 9. These O^+ ions are released from above the southern ionosphere at MLT = 0.0 hr and $L = 5.0$ (Figure 9a), 5.2 (Figure 9b), and 5.4 (Figure 9c) with an initial energy of 10, 25, 50, 100, 250, 500, and 1,000 eV. Since O^+ ions at ≥100 eV are bouncing between the mirror points at multiple times until 07:00 UT, we plot only the first bounce trajectory for them to reduce complexity of figures. Trajectories from the release point to the first northern mirror point are drawn with thick lines and those from the northern to southern mirror point are indicated with thin lines. In a similar way to Figure 3b, displayed are the orbits of

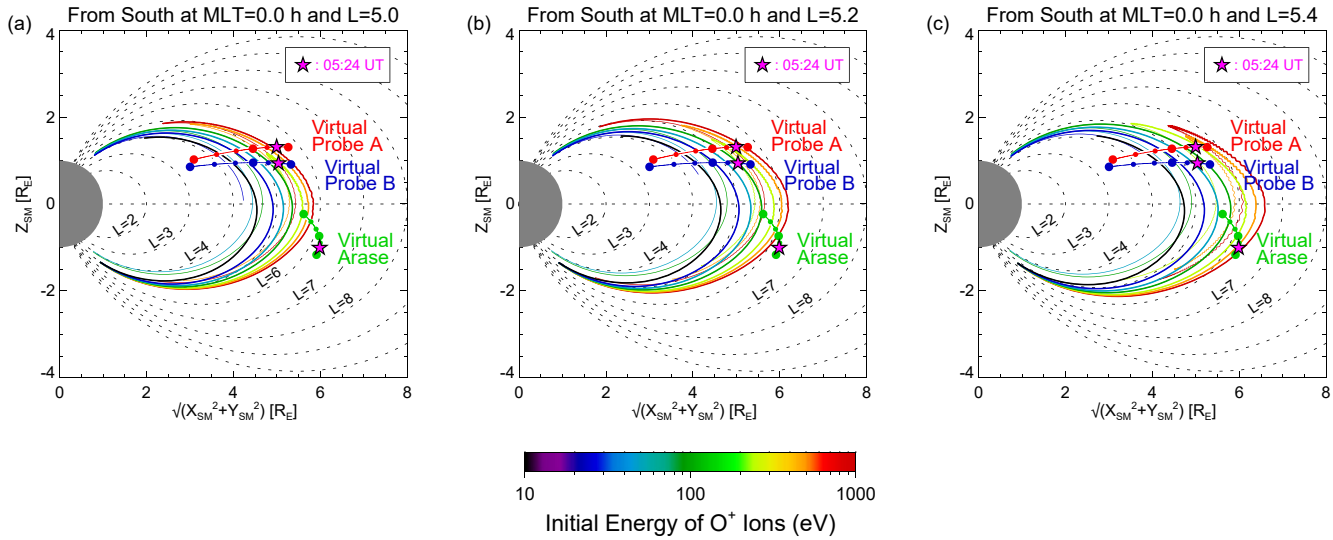

Figure 9. Trajectories of test O^+ ions in the meridional plane before 07:00 UT. These O^+ ions are released from above the southern ionosphere at MLT = 0.0 hr and (a) $L = 5.0$, (b) $L = 5.2$, and (c) $L = 5.4$ with an initial energy of 10, 25, 50, 100, 250, 500, and 1,000 eV. For O^+ ions at ≥100 eV, only the first bounce trajectory is plotted to reduce complexity of figures. Thick lines delineate ion trajectories from the release point to the first northern mirror point and thin lines represent those from the northern to southern mirror point. In a similar way to Figure 3b, the orbital segments of the three virtual satellites are displayed with their locations at substorm onset (05:24 UT, magenta starts).

virtual Arase (green curve), virtual Van Allen Probe A (red curve), and virtual Van Allen Probe B (blue curve) during 05:00–07:00 UT with the locations of the virtual satellites at substorm onset (05:24 UT, magenta starts).

It should be noted that test O^+ ions are launched along the model magnetic field ($\alpha = 80°$) that has a more stretched configuration with Kp = 4. This makes O^+ ions reach in the larger L shell near the equatorial plane ($L \sim 5.5$–6.5) than the initial L shell ($L = 5.0$–5.4), as can be seen in trajectories of O^+ ions of 100–1,000 eV (green to red lines). The convection electric field transports O^+ ions inward by the $E \times B$ drift. The inward motion is more evident for O^+ ions with lower energy because of their smaller velocity along the magnetic field. Thus, O^+ ions of 10–25 eV (black and blue lines) reach the smaller L shell near the equatorial plane ($L \sim 4.5$–5.0).

In the time interval between the substorm onset and 06:30 UT, virtual Arase is flying around $L = 5.9$–6.2 and can observe only O^+ ions with energies higher than ~250 eV launched from $L = 5.4$ (Figure 9c). These O^+ ions appear as the parallel flux from 1 keV to ~100 eV in the energy-time spectrogram (top panel of Figure 8). In the numerical simulation, there are O^+ ions launched from above the northern ionosphere and they have trajectories that are symmetric to Figure 9 against the equatorial plane. These O^+ ions from the northern hemisphere travel longer distance to virtual Arase than those from the southern hemisphere, resulting in more inward drift and a smaller chance to be detected. This would be the reason of the smaller total flux in the antiparallel direction in the energy-time spectrogram (third panel of Figure 8). On the other hand, virtual Van Allen Probe A and Probe B traverse the wider L range from $L \sim 5.5$ to $L \sim 4.0$ to 06:30 UT. Thus, they can observe O^+ ions from 1 keV to 10 eV, as can be seen in Figures 9a–9c. If O^+ ions launched from the northern hemisphere are considered, it is reasonable that the O^+ flux enhancements appear in both parallel and antiparallel directions in the energy-time spectrograms (fourth to ninth panels of Figure 8).

3.4. Destination of FALEO

It is of great interest to examine where FALEOs go after they are detected by satellites. This can be investigated by examining the results of the numerical calculations of O^+ ion trajectories. Figure 10 shows the location of low-energy O^+ ions having the initial energy of 25, 250, 500, and 1,000 eV in the L-MLT plane at 9 different epoch times ($T_{epoch} = 0.5, 1.5, \ldots, 8.5$ hr), where the zero epoch time ($T_{epoch} = 0$ hr) is the beginning of the release of O^+ ions (i.e., 05:27 UT). Just after the release ($T_{epoch} = 0.5$ hr), the low-energy O^+ ions are distributed near the midnight at $L = 4.5$–5.5. This wider distribution of O^+ ions in L is interpreted as the results of the stretched configuration of the model magnetic field and the inward drift by the convection electric field, as discussed in

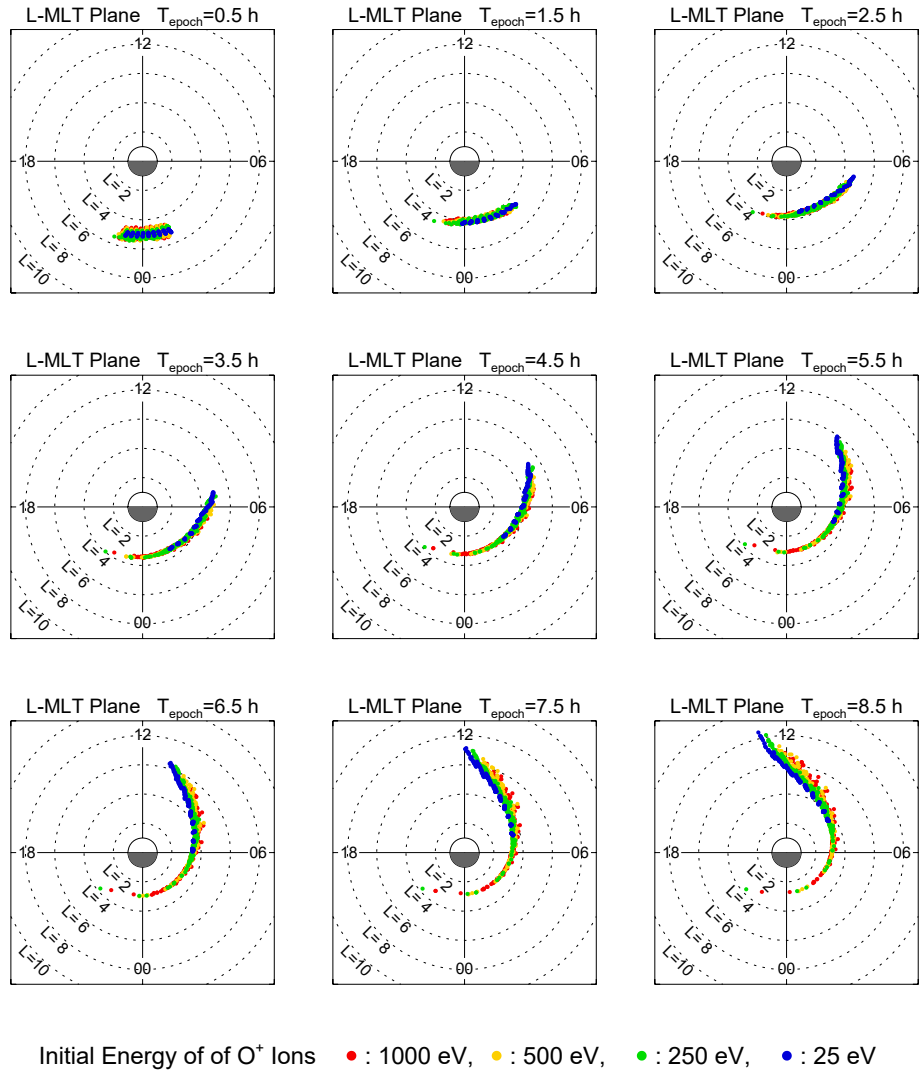

Figure 10. Numerical simulation results of the location of low-energy O^+ ions having the initial energy of 25, 250, 500, and 1,000 eV in the *L*-MLT plane at nine different epoch times (T_{epoch} = 0.5, 1.5, …, 8.5 hr). The zero epoch time (T_{epoch} = 0 hr) is the beginning of the release of O^+ ions (05:27 UT).

aforementioned subsection. Subsequently, during T_{epoch} = 1.5–3.5 hr, O^+ ions are accumulated around L = 3.5–4 and distributed in the midnight to dawn sectors (MLT = 00–06 hr). This is because of their low energy less than 1,000 eV. Such low-energy O^+ ions have a larger $E \times B$ drift velocity due to the corotation electric field than the gradient/curvature drift velocities, resulting in eastward drift. While the corotation $E \times B$ drift velocity (eastward) is independent to O^+ ion energy, the gradient/curvature drift velocity (westward) is smaller for lower energy O^+ ions. Thus, the spatial distribution becomes skewed more eastward for lower energy O^+ ions. Afterward, at T_{epoch} = 4.5–8.5 hr, as the O^+ ions move further eastward, they also drift sunward due to the convection electric field. It is found that FALEOs form a wide and elongated distribution at $L \sim$ 3–8 centered around the dawn to morning sectors in 3–9 hr after substorm onset.

4. Discussion and Conclusions

4.1. Comparison Between Satellite Observations and Numerical Simulation Results

As seen in Figures 4–6, Arase, Probe A, and Probe B simultaneously observe FALEO, whose characteristics are consistent with those reported by previous studies: (a) unidirectional/bidirectional flux enhancement, (b)

Table 2
Start Time of FALEO Flux Enhancement at 1 keV

Satellite	Flux direction	Observations	Simulations
Arase	Parallel	~05:40 UT	05:35–05:45 UT
	Antiparallel	–	05:38–05:46 UT[a]
Probe A	Parallel	~05:45 UT	05:43–05:47 UT
	Antiparallel	~05:42 UT	05:37–05:42 UT
Probe B	Parallel	~05:35 UT	05:35–05:40 UT
	Antiparallel	~05:33 UT	05:32–05:38 UT

[a]Overall flux in the antiparallel direction is 3.2 times lower than that in the parallel direction.

energy-dispersion from a few keV to 10–100 eV, (c) a few minutes delay from substorm onset, (d) dependence of flux direction on satellite position relative to the geomagnetic equator. Table 2 summarizes the start time of FALEO flux enhancement at 1 keV, which was identified from Figure 7 (Section 2.6).

We perform the numerical calculation of test O^+ ion trajectories and create the energy-time spectrograms observed by virtual satellites as shown in Figure 8. It is found that FALEO clearly appears in the energy-time spectrograms with typical characteristics that are quite consistent with those of the real observations (a)–(d). The start time of FALEO flux enhancement at 1 keV is identified from Figure 8 (Section 3.2) and listed in Table 2. Comparison reveals that the start time of FALEO in the numerical simulation is consistent with that in the observations. We consider that the numerical simulation reproduces surprisingly well the observations.

4.2. FALEO as Possible Source of Warm Plasma Cloak and Oxygen Torus

Warm plasma cloak consists of low-energy plasma in the energy range of a few eV to >400 eV that has bidirectional field-aligned distribution, and it is found outside the plasmapause around the dawn to morning (Chappell et al., 2008; Foster & Erickson, 2021; Lee & Angelopoulos, 2014). Oxygen torus is composed of very low-energy oxygen ions with <50 eV (Chappell, 1982; Comfort et al., 1988; Horwitz et al., 1984, 1986, 1990) and its spatial distribution is skewed toward the dawn near the plasmapause (Nosé et al., 2018, 2020; Roberts et al., 1987).

From Figure 10, we find that FALEOs with the initial energy of 25, 250, 500, and 1,000 eV are distributed at $L \sim 3.5$–4 around the dawn and in the wider L range ($L \sim 3$–8) from the morning to the noon. For a direct comparison of the numerical simulation results with the previous observational results, we compute the pseudo flux of O^+ ions integrated over the energy range less than 400 eV. Figure 11 gives its spatial distribution in the L-MLT plane at every 1 hr time interval. The spatial distributions at $T_{epoch} = 3$–9 hr are quite similar to those of the warm plasma cloak and the oxygen torus, suggesting that FALEO is likely to contribute to the formation of those cold ion populations, as insisted by Gkioulidou et al. (2019) and Nosé et al. (2021).

One may consider from Figure 11 that low-energy O^+ ions have only a transient distribution in the MLT range from the dawn to morning. It may be true that the warm plasma cloak and the oxygen torus have a lifetime of <10 hr, if a single substorm is considered. However, substorms can occur intermittently with a recurrent time of 2–4 hr (e.g., Borovsky & Yakymenko, 2017; Morley et al., 2009) during an interval of solar-wind driving of the magnetosphere. This recurrent occurrence will keep the supply of FALEOs into the inner magnetosphere for a long time, enabling the warm plasma cloak and the oxygen torus to survive for more than 10 hr. Previous studies have shown that the oxygen torus is frequently observed during the storm recovery phase (Horwitz et al., 1984; Nosé et al., 2011; Roberts et al., 1987). The preference of the oxygen torus to the storm recovery phase may be interpreted as follows: a number of substorms occur during the storm main phase and provide FALEOs in the inner magnetosphere until the peak of the storm; then the FALEOs evolve into the oxygen torus during the subsequent recovery phase.

5. Conclusions

This study has examined the flux enhancement of the field-aligned low-energy O^+ ion (FALEO) observed simultaneously by three satellites, Arase, Van Allen Probes A and B, during 05:00–07:00 UT on 22 September 2018. The three satellites were situated in the nightside magnetosphere at $L = 3.4$–6.3 and MLT = 23.6–2.8 hr. Arase was located below the geomagnetic equator (GMLAT = −11.2° to −2.4°), while Probe A and B are located above the geomagnetic equator (GMLAT = −9.7° to −18.3°). After a ground substorm signature at 05:24 UT, the three satellites detected the magnetic dipolarization ($\Delta H > 0$ and $|\Delta V| < 0$) at 05:27 UT as well as FALEO with approximately 10–20 min delay. FALEO observed by Arase appeared with the energy-dispersion signatures starting from a few keV to ~100 eV only in the direction parallel to the magnetic field. Whereas, FALEO observed by Probes A and B appeared from a few keV down to 10 eV in the both parallel and antiparallel directions, and echoed a few times, showing the multiband structure in the energy-time spectrograms. The antiparallel flux appeared 2–3 min earlier than the parallel flux. The start times of FALEO are summarized in Table 2. These observational results

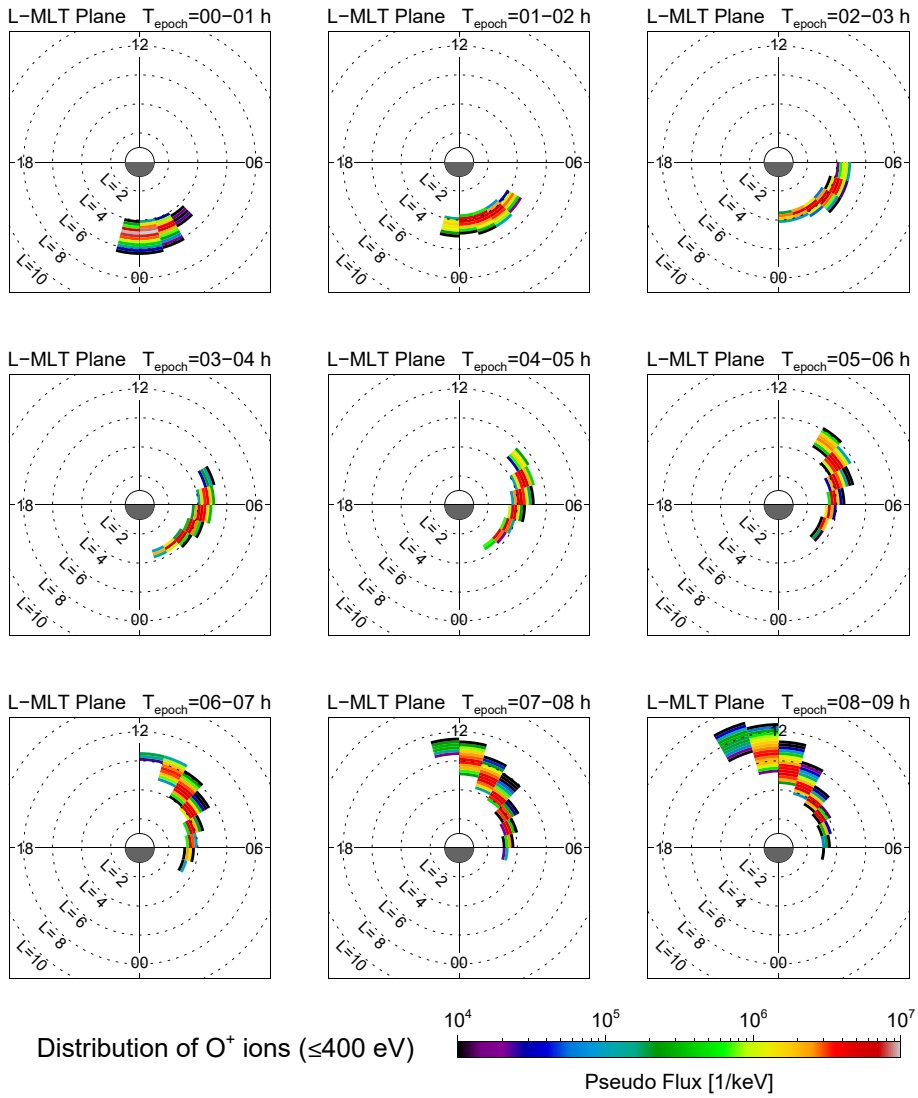

Figure 11. Numerical simulation results of the spatial distribution of O^+ ions in the *L*-MLT plane. Displayed is the pseudo flux of O^+ ions integrated over the energy range less than 400 eV. Each panel shows the distribution at every 1 hr time interval after the release of O^+ ions ($T_{epoch} = 0$ hr).

lead us to suppose that FALEOs are ionospheric O^+ ions that have been extracted from the upper ionosphere in association with substorm onset and flow along the magnetic field toward the geomagnetic equator.

To test this supposition and to investigate where FALEOs drift after detected by satellites, we conducted numerical calculation of O^+ ion trajectories by integrating the guiding center equations of motion. As shown in Table 1, initial parameters of test O^+ ions are given to reproduce the ionospheric ions that are lifted up by ionospheric heating due to the substorm at 05:24 UT and are further accelerated by electromagnetic disturbances in the perpendicular direction to flow out from above the ionosphere between 05:27 UT and 05:39 UT. Some test O^+ ions are detected by virtual satellites that move along the same orbits as the real satellites (i.e., Arase, Probe A, and Probe B), providing energy-time spectrograms as observed by the virtual satellites. There was a quite good agreement between the virtual energy-time spectrograms and the observed energy-time spectrograms for all three satellites, which indicates the correctness of the above supposition. It was found that test O^+ ions with the energy less than 400 eV are distributed in the midnight to morning sectors (MLT = 00–09 hr) near the plasmapause ($L = 3.5$–5) in 2–5 hr after their launch from above the ionosphere, and then move to the morning to noon sectors around $L = 3$–8. This spatial distribution and energy range are consistent with those of the warm plasma cloak

and the oxygen torus reported by previous studies. We therefore conclude that FALEO is a likely source of the warm plasma cloak and the oxygen torus.

Data Availability Statement

Science data of the ERG (Arase) satellite were obtained from the ERG Science Center (Miyoshi, Hori, et al., 2018) operated by ISAS/JAXA and ISEE/Nagoya University (https://ergsc.isee.nagoya-u.ac.jp/index.shtml.en). The present study analyzed the Orbit-L2 v03 data, the MGF-L2 v03.04 data, and the LEPi-L2 v03_00 data. The Van Allen Probes/EMFISIS and ECT-HOPE data are available at https://emfisis.physics.uiowa.edu/and https://rbsp-ect.newmexicoconsortium.org/, respectively. The present study used the EMFISIS L3_v1.7.1 and HOPE rel04_L3_v.7.0.0 data for Probe A and the EMFISIS L3_v1.6.2 and HOPE rel04_L3_v.7.0.0 data for Probe B. The Wp index is available at https://doi.org/10.17593/13437-46800. The SYM-H index is provided by the World Data Center for Geomagnetism, Kyoto, and is available at http://wdc.kugi.kyoto-u.ac.jp/. The Kp index was provided by J. Matzka at the Helmholtz Centre Potsdam, GFZ German Research Centre for Geosciences, and is available at https://doi.org/10.5880/Kp.0001. The SML index and ground magnetic field data are available at https://supermag.jhuapl.edu/.

Acknowledgments
We gratefully acknowledge the SuperMAG collaborators (CANMOS, CARISMA, THEMIS). Geomagnetic fields of the IGRF-13 and T89 models were calculated with GEOPACK routines developed by N. A. Tsyganenko and coded by H. Korth. The numerical simulation code for ion trajectories was provided by D. C. Delcourt. The numerical simulation was performed using the CIDAS-computer system of the Institute for Space-Earth Environmental Research, Nagoya University. This study is supported by the Japan Society for the Promotion of Science (JSPS), Grant-in-Aid for Scientific Research (B; Grant 16H04057 and 21H01147), Challenging Research (Pioneering; Grant 17K18804), and Grant-in-Aid for Specially Promoted Research (Grant 16H06286); as well as Ito Kagaku Shinkou Kai and Yamada Kagaku Shinkou Zaidan. Y. M. is supported by the Japan Society for the Promotion of Science (JSPS), Grant-in-Aid for Scientific Research on Innovative Areas (Grant 15H05815) and Grant-in-Aid for Scientific Research (B; Grant 20H01959).

References

Alken, P., Thébault, E., Beggan, C. D., Amit, H., Aubert, J., Baerenzung, J., et al. (2021). International Geomagnetic Reference Field: The thirteenth generation. *Earth Planets and Space*, *73*, 49. https://doi.org/10.1186/s40623-020-01288-x

Asamura, K., Kazama, Y., Yokota, S., Kasahara, S., & Miyoshi, Y. (2018). Low-energy particle experiments-ion mass analyzer (LEPi) onboard the ERG (Arase) satellite. *Earth Planets and Space*, *70*, 70. https://doi.org/10.1186/s40623-018-0846-0

Asamura, K., Miyoshi, Y., & Shinohara, I. (2018). *The LEPi instrument Level-2 3D flux data of exploration of energization and radiation in Geospace (ERG) Arase satellite, Version v03_00*. ERG Science Center, Institute for Space-Earth Environmental Research, Nagoya University. https://doi.org/10.34515/DATA.ERG-05000

Birn, J., Thomsen, M. F., Borovsky, J. E., Reeves, G. D., McComas, D. J., Belian, R. D., & Hesse, M. (1997). Substorm ion injections: Geosynchronous observations and test particle orbits in three-dimensional dynamic MHD fields. *Journal of Geophysical Research*, *102*(A2), 2325–2341. https://doi.org/10.1029/96JA03032

Birn, J., Thomsen, M. F., Borovsky, J. E., Reeves, G. D., McComas, D. J., Belian, R. D., & Hesse, M. (1998). Substorm electron injections: Geosynchronous observations and test particle simulations. *Journal of Geophysical Research*, *103*(A5), 9235–9248. https://doi.org/10.1029/97JA02635

Borovsky, J. E., & Yakymenko, K. (2017). Substorm occurrence rates, substorm recurrence times, and solar wind structure. *Journal of Geophysical Research*, *122*, 2973–2998. https://doi.org/10.1002/2016JA023625

Chappell, C. R. (1982). Initial observations of thermal plasma composition and energetics from Dynamics Explorer-1. *Geophysical Research Letters*, *9*(9), 929–932. https://doi.org/10.1029/GL009i009p00929

Chappell, C. R., Huddleston, M. M., Moore, T. E., Giles, B. L., & Delcourt, D. C. (2008). Observations of the warm plasma cloak and an explanation of its formation in the magnetosphere. *Journal of Geophysical Research*, *113*, A09206. https://doi.org/10.1029/2007JA012945

Chaston, C. C., Bonnell, J. B., Carlson, C. W., McFadden, J. P., Ergun, R. E., & Lund, E. J. (2004). Auroral ion acceleration in dispersive Alfvén waves. *Journal of Geophysical Research*, *109*, A04205. https://doi.org/10.1029/2003JA010053

Chaston, C. C., Bonnell, J. W., Wygant, J. R., Kletzing, C. A., Reeves, G. D., Gerrard, A., et al. (2015). Extreme ionospheric ion energization and electron heating in Alfvén waves in the storm time inner magnetosphere. *Geophysical Research Letters*, *42*, 10531–10540. https://doi.org/10.1002/2015GL066674

Chaston, C. C., Peticolas, L. M., Carlson, C. W., McFadden, J. P., Mozer, F., Wilberand, M., et al. (2005). Energy deposition by Alfvén waves into the dayside auroral oval: Cluster and FAST observations. *Journal of Geophysical Research*, *110*, A02211. https://doi.org/10.1029/2004JA010483

Comfort, R. H., Newberry, I. T., & Chappell, C. R. (1988). Preliminary statistical survey of plasmaspheric ion properties from observations by DE 1/RIMS. In T. E.Moore, J. H.Waite, T. W.Moorehead, & W. B.Hanson (Eds.), *Modeling magnetospheric plasma*. *Geophysical Monograph Series* (Vol. 44, pp. 107–114). American Geophysical Union. https://doi.org/10.1029/GM044p0107

Delcourt, D. C., Sauvaud, J. A., & Pedersen, A. (1990). Dynamics of single-particle orbits during substorm expansion phase. *Journal of Geophysical Research*, *95*(A12), 20853–20865. https://doi.org/10.1029/JA095iA12p20853

Delzanno, G. L., Borovsky, J. E., Henderson, M. G., Lira, P. A. R., Roytershteyn, V., & Welling, D. T. (2021). The impact of cold electrons and cold ions in magnetospheric physics. *Journal of Atmospheric and Solar-Terrestrial Physics*, *220*, 105599. https://doi.org/10.1016/j.jastp.2021.105599

Fernandes, P. A., Larsen, B. A., Thomsen, M. F., Skoug, R. M., Reeves, G. D., Denton, M. H., et al. (2017). The plasma environment inside geostationary orbit: A Van Allen Probes HOPE survey. *Journal of Geophysical Research: Space Physics*, *122*, 9207–9227. https://doi.org/10.1002/2017JA024160

Foster, J. C., & Erickson, P. J. (2021). Van Allen Probes observations of oxygen ions at the geospace plume. *Frontiers in Astronomy and Space Sciences*, *8*, 705637. https://doi.org/10.3389/fspas.2021.705637

Funsten, H. O., Skoug, R. M., Guthrie, A. A., MacDonald, E. A., Baldonado, J. R., Harper, R. W., et al. (2013). Helium, oxygen, proton, and electron (HOPE) mass spectrometer for the Radiation Belt storm Probes mission. *Space Science Reviews*, *179*, 423–484. https://doi.org/10.1007/s11214-013-9968-7

Fuselier, S. A., Collin, H. L., Ghielmetti, A. G., Claflin, E. S., Moore, T. E., Collier, M. R., et al. (2002). Localized ion outflow in response to a solar wind pressure pulse. *Journal of Geophysical Research*, *107*(A8), 1203. https://doi.org/10.1029/2001JA000297

Gjerloev, J. W. (2012). The SuperMAG data processing technique. *Journal of Geophysical Research*, *117*, A09213. https://doi.org/10.1029/2012JA017683

Gkioulidou, M., Ohtani, S., Ukhorskiy, A. Y., Mitchell, D. G., Takahashi, K., Spence, H. E., et al. (2019). Low-energy (<keV) O^+ ion outflow directly into the inner magnetosphere: Van Allen Probes observations. *Journal of Geophysical Research: Space Physics*, *124*, 405–419. https://doi.org/10.1029/2018JA025862

Horwitz, J. L., Comfort, R. H., Brace, L. H., & Chappell, C. R. (1986). Dual-spacecraft measurements of plasmasphere-ionosphere coupling. *Journal of Geophysical Research*, *91*(A10), 11203–11216. https://doi.org/10.1029/JA091iA10p11203

Horwitz, J. L., Comfort, R. H., & Chappell, C. R. (1984). Thermal ion composition measurements of the formation of the new outer plasmasphere and double plasmapause during storm recovery phase. *Geophysical Research Letters*, *11*(8), 701–704. https://doi.org/10.1029/GL011i008p00701

Horwitz, J. L., Comfort, R. H., Richards, P. G., Chandler, M. O., Chappell, C. R., Anderson, P., et al. (1990). Plasmasphere-ionosphere coupling 2: Ion composition measurements at plasmaspheric and ionospheric altitudes and comparison with modeling results. *Journal of Geophysical Research*, *95*(A6), 7949–7959. https://doi.org/10.1029/JA095iA06p07949

Hull, A. J., Chaston, C. C., Bonnell, J. W., Damiano, P. A., Wygant, J. R., & Reeves, G. D. (2020). Correlations between dispersive Alfvén wave activity, electron energization, and ion outflow in the inner magnetosphere. *Geophysical Research Letters*, *47*, e2020GL088985. https://doi.org/10.1029/2020GL088985

Hull, A. J., Chaston, C. C., Bonnell, J. W., Wygant, J. R., Kletzing, C. A., Reeves, G. D., & Gerrard, A. (2019). Dispersive Alfvén wave control of O^+ ion outflow and energy densities in the inner magnetosphere. *Geophysical Research Letters*, *46*, 8597–8606. https://doi.org/10.1029/2019GL083808

Iyemori, T., Araki, T., Kamei, T., & Takeda, M. (1992). Mid-latitude geomagnetic indices ASY and SYM (provisional), no. 1, 1989–1990. In *Data analysis center for geomagnetism and space magnetism*. Kyoto University.

Jahn, J.-M., Goldstein, J., Reeves, G. D., Fernandes, P. A., Skoug, R. M., Larsen, B. A., & Spence, H. E. (2017). The warm plasma composition in the inner magnetosphere during 2012–2015. *Journal of Geophysical Research: Space Physics*, *122*, 11018–11043. https://doi.org/10.1002/2017JA024183

Khan, H., Collier, M. R., & Moore, T. E. (2003). Case study of solar wind pressure variations and neutral atom emissions observed by IMAGE/LENA. *Journal of Geophysical Research*, *108*(A12), 1422. https://doi.org/10.1029/2003JA009977

Kistler, L. M., Mouikis, C. G., Spence, H. E., Menz, A. M., Skoug, R. M., Funsten, H. O., et al. (2016). The source of O^+ in the storm time ring current. *Journal of Geophysical Research: Space Physics*, *121*, 5333–5349. https://doi.org/10.1002/2015JA022204

Kletzing, C. A., Kurth, W. S., Acuna, M., MacDowall, R. J., Torbert, R. B., Averkamp, T., et al. (2013). The electric and magnetic field instrument suite and integrated science (EMFISIS) on RBSP. *Space Science Reviews*, *179*(1–4), 127–181. https://doi.org/10.1007/s11214-013-9993-6

Lee, J. H., & Angelopoulos, V. (2014). On the presence and properties of cold ions near Earth's equatorial magnetosphere. *Journal of Geophysical Research: Space Physics*, *119*, 1749–1770. https://doi.org/10.1002/2013JA019305

Matsuoka, A., Teramoto, M., Imajo, S., Kurita, S., Miyoshi, Y., & Shinohara, I. (2018). *The MGF instrument Level-2 spin-fit magnetic field data of Exploration of energization and Radiation in Geospace (ERG) Arase satellite, Version v03.04*. ERG Science Center, Institute for Space-Earth Environmental Research, Nagoya University. https://doi.org/10.34515/DATA.ERG-06001

Matsuoka, A., Teramoto, M., Nomura, R., Nosé, M., Fujimoto, A., Tanaka, Y., et al. (2018). The Arase (ERG) magnetic field investigation. *Earth Planets and Space*, *70*, 43. https://doi.org/10.1186/s40623-018-0800-1

Matzka, J., Bronkalla, O., Tornow, K., Elger, K., & Stolle, C. (2021). *Geomagnetic Kp index. V. 1.0*. GFZ Data Services. https://doi.org/10.5880/Kp.0001

Matzka, J., Stolle, C., Yamazaki, Y., Bronkalla, O., & Morschhauser, A. (2021). The geomagnetic Kp index and derived indices of geomagnetic activity. *Space Weather*, *19*, e2020SW002641. https://doi.org/10.1029/2020SW002641

Mauk, B. H. (1986). Quantitative modeling of the "convection surge" mechanism of ion acceleration. *Journal of Geophysical Research*, *91*(A12), 13423–13431. https://doi.org/10.1029/JA091iA12p13423

Mauk, B. H., Fox, N. J., Kanekal, S. G., Kessel, R. L., Sibeck, D. G., & Ukhorskiy, A. (2013). Science objectives and rationale for the Radiation Belt storm Probes mission. *Space Science Reviews*, *179*(1–4), 3–27. https://doi.org/10.1007/s11214-012-9908-y

Maynard, N. C., & Chen, A. J. (1975). Isolated cold plasma regions—Observations and their relation to possible production mechanisms. *Journal of Geophysical Research*, *80*, 1009–1013. https://doi.org/10.1029/JA080i007p01009

Miyoshi, Y., Hori, T., Shoji, M., Teramoto, M., Chang, T.-F., Segawa, T., et al. (2018). The ERG science center. *Earth Planets and Space*, *70*, 96. https://doi.org/10.1186/s40623-018-0867-8

Miyoshi, Y., Shinohara, I., & Jun, C.-W. (2018). *The Level-2 orbit data of Exploration of energization and Radiation in geospace (ERG) Arase satellite, Version v03*. ERG Science Center, Institute for Space-Earth Environmental Research, Nagoya University. https://doi.org/10.34515/DATA.ERG-12000

Miyoshi, Y., Shinohara, I., Takashima, T., Asamura, K., Higashio, N., Mitani, T., et al. (2018). Geospace Exploration Project ERG. *Earth Planets and Space*, *70*, 101. https://doi.org/10.1186/10.1186/s40623-018-0862-0

Möbius, E., Scholer, M., Klecker, B., Hovestadt, D., Gloeckler, G., & Ipavich, F. M. (1987). Acceleration of ions of ionospheric origin in the plasma sheet during substorm activity. In A. T. Y. Lui (Ed.), *Magnetotail physics* (pp. 231–234).

Morley, S. K., Rouillard, A. P., & Freeman, M. P. (2009). Recurrent substorm activity during the passage of a corotating interaction region. *Journal of Atmospheric and Solar-Terrestrial Physics*, *71*, 1073–1081. https://doi.org/10.1016/j.jastp.2008.11.009

Nagai, T. (1991). An empirical model of substorm-related magnetic field variations at synchronous orbit. In J. R.Kan, T. A.Potemra, S.Kokubun, & T.Iijima (Eds.), *Magnetospheric substorms* (pp. 91–95). https://doi.org/10.1029/GM064p0091

Nagai, T., Ondoh, T., Matsumoto, H., Goka, T., Fukuda, T., Nosé, M., et al. (1996). ETS-VI magnetic field observations of the near-Earth magnetotail during substorms. *Journal of Geomagnetism and Geoelectricity*, *48*, 741–748. https://doi.org/10.5636/jgg.48.741

Newell, P. T., & Gjerloev, J. W. (2011a). Evaluation of SuperMAG auroral electrojet indices as indicators of substorms and auroral power. *Journal of Geophysical Research*, *116*, A12211. https://doi.org/10.1029/2011JA016779

Newell, P. T., & Gjerloev, J. W. (2011b). Substorm and magnetosphere characteristic scales inferred from the SuperMAG auroral electrojet indices. *Journal of Geophysical Research*, *116*, A12232. https://doi.org/10.1029/2011JA016936

Nosé, M., Iyemori, T., Wang, L., Hitchman, A., Matzka, J., Feller, M., et al. (2012). Wp index: A new substorm index derived from high-resolution geomagnetic field data at low latitude. *Space Weather*, *10*, S08002. https://doi.org/10.1029/2012SW000785

Nosé, M., Keika, K., Kletzing, C. A., Spence, H. E., Smith, C. W., MacDowall, R. J., et al. (2016). Van Allen Probes observations of magnetic field dipolarization and its associated O^+ flux variations in the inner magnetosphere at $L < 6.6$. *Journal of Geophysical Research: Space Physics*, *121*, 7572–7589. https://doi.org/10.1002/2016JA022549

Nosé, M., Matsuoka, A., Kumamoto, A., Kasahara, Y., Goldstein, J., Teramoto, M., et al. (2018). Longitudinal structure of oxygen torus in the inner magnetosphere: Simultaneous observations by Arase and Van Allen Probe A. *Geophysical Research Letters*, *45*, 10177–10184. https://doi.org/10.1029/2018GL080122

Nosé, M., Matsuoka, A., Kumamoto, A., Kasahara, Y., Teramoto, M., Kurita, S., et al. (2020). Oxygen torus and its coincidence with EMIC wave in the deep inner magnetosphere: Van Allen Probe B and Arase observations. *Earth Planets and Space*, *72*, 111. https://doi.org/10.1186/s40623-020-01235-w

Nosé, M., Matsuoka, A., Miyoshi, Y., Asamura, K., Hori, T., Teramoto, M., et al. (2021). Field-aligned low-energy O^+ flux enhancements in the inner magnetosphere observed by Arase. *Journal of Geophysical Research*, *126*, e2021JA029168. https://doi.org/10.1002/2021JA029168

Nosé, M., Taguchi, S., Christon, S. P., Collier, M. R., Moore, T. E., Carlson, C. W., & McFadden, J. P. (2009). Response of ions of ionospheric origin to storm time substorms: Coordinated observations over the ionosphere and in the plasma sheet. *Journal of Geophysical Research*, *114*, A05207. https://doi.org/10.1029/2009JA014048

Nosé, M., Takahashi, K., Anderson, R. R., & Singer, H. J. (2011). Oxygen torus in the deep inner magnetosphere and its contribution to recurrent process of O^+-rich ring current formation. *Journal of Geophysical Research*, *116*, A10224. https://doi.org/10.1029/2011JA016651

Ogawa, Y., Sawatsubashi, M., Buchert, S. C., Hosokawa, K., Taguchi, S., Nozawa, S., et al. (2013). Relationship between auroral substorm and ion upflow in the nightside polar ionosphere. *Journal of Geophysical Research: Space Physics*, *118*, 7426–7437. https://doi.org/10.1002/2013JA018965

Roberts, W. T., Jr., Horwitz, J. L., Comfort, R. H., Chappell, C. R., Waite, J. H., Jr., & Green, J. L. (1987). Heavy ion density enhancements in the outer plasmasphere. *Journal of Geophysical Research*, *92*(A12), 13499–13512. https://doi.org/10.1029/JA092iA12p13499

Sánchez, E. R., Mauk, B. H., & Meng, C.-I. (1993). Adiabatic vs. non-adiabatic particle distributions during convection surges. *Geophysical Research Letters*, *20*, 177–180. https://doi.org/10.1029/93GL00237

Shen, Y., & Knudsen, D. J. (2020). On O^+ ion heating by BBELF waves at low altitude: Test particle simulations. *Journal of Geophysical Research: Space Physics*, *125*, e2019JA027291. https://doi.org/10.1029/2019JA027291

Spence, H. E., Reeves, G. D., Baker, D. N., Blake, J. B., Bolton, M., Bourdarie, S., et al. (2013). Science goals and overview of the radiation belt storm probes (RBSP) Energetic particle, composition, and thermal plasma (ECT) suite on NASA's Van Allen Probes mission. *Space Science Reviews*, *179*, 311–336. https://doi.org/10.1007/s11214-013-0007-5

Stern, D. P. (1975). The motion of a proton in the equatorial magnetosphere. *Journal of Geophysical Research*, *80*, 595–599. https://doi.org/10.1029/JA080i004p00595

Strangeway, R. J., Ergun, R. E., Su, Y.-J., Carlson, C. W., & Elphic, R. C. (2005). Factors controlling ionospheric outflows as observed at intermediate altitudes. *Journal of Geophysical Research*, *110*, A03221. https://doi.org/10.1029/2004JA010829

Strangeway, R. J., Russell, C. T., Carlson, C. W., McFadden, J. P., Ergun, R. E., Temerin, M., et al. (2000). Cusp field-aligned currents and ion outflows. *Journal of Geophysical Research*, *105*(A9), 21129–21141. https://doi.org/10.1029/2000JA900032

Tsyganenko, N. A. (1989). A magnetospheric magnetic field model with a warped tail current sheet. *Planetary and Space Science*, *37*, 5–20. https://doi.org/10.1016/0032-0633(89)90066-4

Volland, H. (1973). A semiempirical model of large-scale magnetospheric electric fields. *Journal of Geophysical Research*, *78*(1), 171–180. https://doi.org/10.1029/JA078i001p00171

Wang, C.-P., Zaharia, S. G., Lyons, L. R., & Angelopoulos, V. (2013). Spatial distributions of ion pitch angle anisotropy in the near-Earth magnetosphere and tail plasma sheet. *Journal of Geophysical Research: Space Physics*, *118*, 244–255. https://doi.org/10.1029/2012JA018275

World Data Center for Geomagnetism, Kyoto, & Nosé, M. (2016). *Geomagnetic Wp index*. https://doi.org/10.17593/13437-46800